

Energy budget in the 2017-09-07 “cold” solar flare

GREGORY D. FLEISHMAN,^{1,2} GALINA G. MOTORINA,³ SIJIE YU,¹ AND GELU M. NITA¹

¹*Center For Solar-Terrestrial Research, New Jersey Institute of Technology, Newark, NJ 07102, USA*

²*Institut für Sonnenphysik (KIS), Schöneckstrasse 6, D-79104 Freiburg, Germany*

³*Central Astronomical Observatory at Pulkovo of Russian Academy of Sciences, St. Petersburg, 196140, Russia*

Abstract

A subclass of early impulsive solar flares, cold flares, was proposed to represent a clean case, where the release of the free magnetic energy (almost) entirely goes to acceleration of the nonthermal electrons, while the observed thermal response is entirely driven by the nonthermal energy deposition to the ambient plasma. This paper studies one more example of a cold flare, which was observed by a unique combination of instruments. In particular, this is the first cold flare observed with the Expanded Owens Valley Solar Array and, thus, for which the dynamical measurement of the coronal magnetic field and other parameters at the flare site is possible. With these new data, we quantified the coronal magnetic field at the flare site, but did not find statistically significant variations of the magnetic field within the measurement uncertainties. We estimated that the uncertainty in the corresponding magnetic energy exceeds the thermal and nonthermal energies by an order of magnitude; thus, there should be sufficient free energy to drive the flare. We discovered a very prominent soft-hard-soft spectral evolution of the microwave-producing nonthermal electrons. We computed energy partitions and concluded that the nonthermal energy deposition is likely sufficient to drive the flare thermal response similarly to other cold flares.

Keywords: Sun: Flares - Sun: X-rays, EUV, Radio emission

1. INTRODUCTION

Solar flares are commonly referred to as transient brightenings in the solar atmosphere driven by release of free magnetic energy (Benz 2008). A typical solar flare demonstrates substantial spatial complexity and time variability in both thermal and nonthermal components. This includes multiple episodes of nonthermal particle acceleration and plasma heating—both associated (Neupert effect, Neupert 1968) and not associated (direct heating; see, e.g., Caspi & Lin 2010) with the nonthermal energy deposition. The chain of the magnetic energy conversions to other types of energy such as thermal, nonthermal, and kinetic energies and transformations between them is extremely complex. The flare complexity, spatial and temporal, further complicates understanding of these phenomena and their quantification. Thus, analysis of flares with simple time profiles, for example, single rise-decay shape (single-spike flares), may represent a cleaner case for the flare energy release and budget study compared with other cases.

Often, although not always, the single-spike flares belong to a class of early impulsive flares (Sui et al. 2006) or even to an extreme subclass of “cold” flares (Ly-

senko et al. 2018, 2023). Lysenko et al. (2018) proposed that the cold flares may represent a cleanest case for the study of particle acceleration and their forthcoming thermalization resulting in a thermal response of the ambient plasma. However, several case studies of the cold flares (Fleishman et al. 2016; Motorina et al. 2020) revealed that the spatial structure of the flaring volume was not that simple—it consisted of two distinct (likely, interacting) magnetic flux tubes. In other cases (e.g., Fleishman et al. 2021), more than two flaring loops may be involved. Perhaps, having more than one flux tube is the morphology that facilitates the release of the free magnetic energy to drive the flare.

Quantification of the energy release and forthcoming transformation requires remote diagnostics of the magnetic, thermal, and nonthermal energies (and, in a general case, the kinetic energy as well). While the quantification of the thermal and nonthermal energies has been available from the extreme ultraviolet (EUV) and soft X-ray (SHR) measurements in the former case and from microwave and hard X-ray (HXR) measurements in the latter case, the magnetic energy has been estimated only indirectly—based on coronal extrapolations of the magnetic field measured at the photosphere.

Recently, a new powerful methodology capable of measuring the evolving magnetic field in the coronal flaring loops has been reported (Fleishman et al. 2020), thus, offering a new avenue of estimating the magnetic energy in the flaring volume. This methodology is based on the broadband microwave imaging spectroscopy now available from the Expanded Owens Valley Solar Array (EOVSA, Gary et al. 2018) and, along with the spatially resolved measurements of the magnetic field (Fleishman et al. 2020), also offers maps of the thermal plasma number density and nonthermal electron population (Fleishman et al. 2022).

Here we study a solar flare recorded by EOVSAs on 2017-Sep-07 around 18:41 UT and observed by a handful of other instruments. This flare demonstrates a single main nonthermal peak, although two or three weaker peaks are also present, and formally falls into a category of “cold” flares according to the classification proposed by Lysenko et al. (2023) based on the relationship between the X-ray and microwave fluxes; see Figure 1. We report on multi-instrument observations of this flare, quantification of its thermal and nonthermal energies with the EUV, SXR, and HXR diagnostics, physical parameter maps derived from the microwave diagnostics, and devise a 3D model of the flare.

2. OBSERVATIONS

The solar flare SOL2017-09-07T184140, GOES class C4.5, occurred at $\sim 18:41$ UT in AR 12673 with $\beta\gamma$ -configuration located at W770S208 just after a C5.2 class flare which ended at 18:36 UT in the same AR. The flare displayed several peaks, the main of which had a short impulsive profile with a peak at $\sim 18:41:40$ UT in hard X-ray (HXR) above 20 keV and in microwaves that lasted about 20 s. This short impulsive event shares some properties of nonthermally-dominated (‘cold’) solar flares (Motorina et al. 2020) and it is the first of them for which microwave imaging spectroscopy data from EOVSAs were available.

2.1. Overview of the instruments used in the analysis and gaps in the data

This flare was observed with a unique combination of space- and ground-based instruments throughout the entire electromagnetic spectrum, from radio waves to X-rays, see Figure 1. The spectral X-ray data are available from the Gamma-ray Burst Monitor (GBM) on board of the Fermi Gamma-ray Space Telescope (*Fermi*/GBM; Meegan et al. 2009) and *Konus-Wind* (Aptekar et al. 1995), while *RHESSI* (Lin et al. 2002) data are only available in the late decay phase, and are not too useful in this case. The *Fermi*/GBM and *Konus-Wind* light

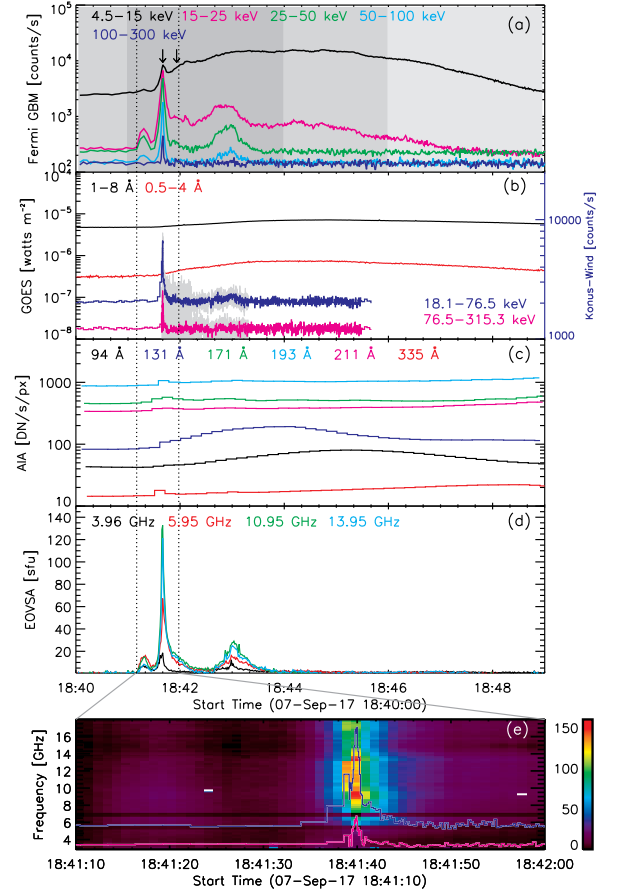


Figure 1. Overview of the 2017-Sep-07 flare. From top to bottom: (a) *Fermi*/GBM light curves at several energy ranges indicated by the legend. The gray—dark gray—gray—light gray areas indicate the breakdown onto the time ranges, where the model spectral fitting of the *Fermi*/GBM data was performed using averaging over, respectively, 20—4—20—60 s time intervals. Vertical arrows point on time frames, where the *Fermi*/GBM spectra and fits are shown in Figure 3 (middle and right panels); (b) low and high *GOES* channels and G1 and G2 *Konus-Wind* light curves. The full resolution *Konus-Wind* light curves are shown in light gray. To reduce the statistical fluctuations the light curves were averaged to 256 ms after the burst, observed with 16 ms time cadence. The averaged light curves are shown in blue and scarlet; (c) *SDO*/AIA light curves, for six passbands indicated in the panel, obtained from the selected ROI (see Figure 2); (d) EOVSAs light curves at several microwave frequencies indicated with the legend; (e) EOVSAs dynamic spectrum of the impulsive flare phase with overlaid *Konus-Wind* light curves plotted in arbitrary units. Vertical dotted lines in panels (a-d) indicate the impulsive phase shown in the (e) panel.

curves are shown in Figure 1(a) and Figure 1(b), respectively. Contextual soft X-ray data from the Geostationary Operational Environmental Satellite (*GOES*; White et al. 2005) are available (Figure 1(b)). In the EUV do-

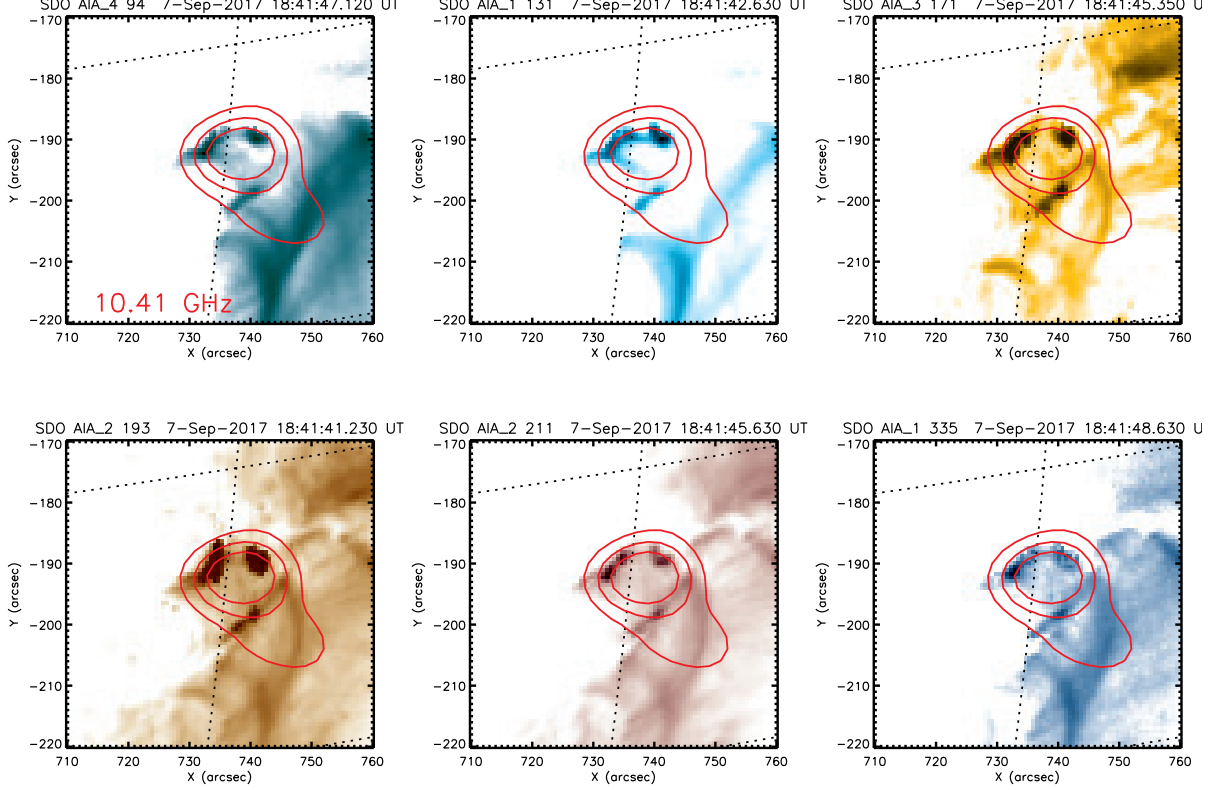


Figure 2. AIA maps taken during the impulsive phase of the September 07, 2017 flare with overlaid EOVSA map 30, 50, and 70% contours at 10.41 GHz (red lines) taken at 18:41:39.5 UT, which corresponds to the maximum of the microwave emission.

main, *Solar Dynamics Observatory*/Atmospheric Imaging Assembly (*SDO*/AIA; Lemen et al. 2012) data are available to quantify the thermal properties of the flaring plasma. The EUV light curves integrated over the region of interest (ROI; see Figure 2) are shown in Figure 1(c). Unique data, not available for the cold solar flares studied before, but available in our case, are the microwave imaging spectroscopy data from EOVSA and, thus, the corresponding data products such as evolving parameter maps (Fleishman et al. 2020, 2022). The EOVSA light curves and the dynamic spectrum are shown in Figure 1(d, e). The data presented in Figure 1 permit us to estimate the increase of the GOES flux, $\Delta GOES \simeq 4.9 \times 10^{-7} \text{ W m}^{-2}$, during the flare impulsive phase, and to compare it with the microwave peak flux of 150 sfu at 9.4 GHz, which confidently places this flare in the category of the cold ones; cf. figure 11 in Lysenko et al. (2023).

2.2. X-ray data

Hard X-ray observations of the impulsive phase of the flare are only accessible from *Fermi*/GBM and *Konus-Wind*. The *Fermi*/GBM light curves (see Figure 1(a)) show several peaks, where the second one at

$\sim 18:41:39.7$ UT is associated with the main peak of the microwave emission.

Konus-Wind recorded the impulsive phase of the flare in the G1 and G2 channels both in the waiting and trigger modes, where its trigger time at the Earth center was 18:41:39.64 UT. The *Konus-Wind* count rate (see Figure 1(b)) had quite high background level during the flare. Thus, *Konus-Wind* didn't see the weaker peak seen by *Fermi*/GBM. The HXR peak time seen by *Konus-Wind* in the 18.1–76.5 keV range was at 18:41:39.9 UT, which will be referred as the HXR peak time further in the text.

GOES soft X-ray (SXR) data are shown in Figure 1(b). There is slight enhancement seen in both low and high energy channels at $\sim 18:41$ UT, which is roughly co-temporal with *SDO*/AIA enhancement seen in the time profiles in Figure 1(c).

2.3. EUV: *SDO*/AIA data

The EUV full solar disk data set is available in six *SDO*/AIA (94, 131, 171, 193, 211, 335 Å) coronal passbands. The AIA images with high $\sim 1.2''$ spatial and 12 s temporal resolution have been calibrated to level 1.5 using the *aia_prep* routine in SSWIDL and nor-

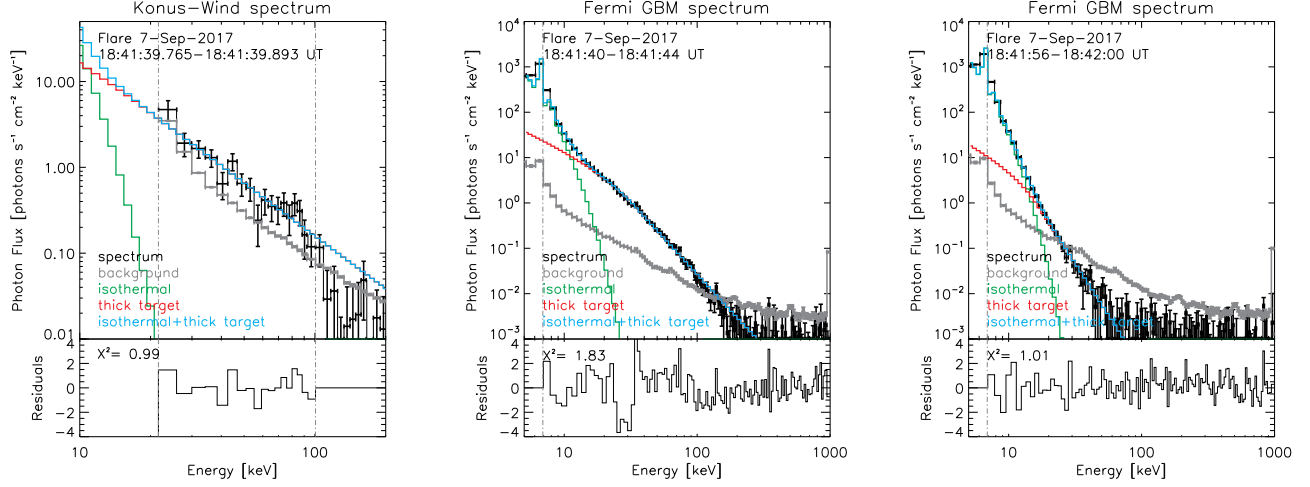


Figure 3. Examples of the *Konus-Wind* and *Fermi*/GBM fits (blue histogram) with isothermal (green histogram) plus thick target model (red histogram) during the nonthermal peak at 18:41:39 UT (left panel) and later 18:41:40–18:41:44 UT, 18:41:56–18:42:00 UT (middle and right panels). The X-ray averaged data and the background level are shown with black and gray histograms respectively. Bottom panels indicate residuals.

malized by the exposure time. There was almost no saturation of the AIA data during the flare. The saturation effects are included in further analysis of the AIA data. We investigate the EUV emission from the ROI shown in Figure 2 to estimate the thermal energy of the flare plasma and its evolution in the coronal part. To infer the integral plasma properties, we use the Differential Emission Measure (DEM) technique (Hannah & Kontar 2012) applied to the entire ROI. To derive spatially resolved plasma parameters (temperature and emission measure), we employ the DEM maps (Hannah & Kontar 2013) with the methodology developed by Motorina et al. (2020) and earlier applied to two solar flares: SOL2013-11-05T035054 and SOL2014-02-16T064600 (Motorina et al. 2020; Fleishman et al. 2021).

2.4. MW data

This event has been imaged using EOVSa at 134 frequencies, across 31 spectral windows from 3 to 18 GHz, following the methods used by Fleishman et al. (2020), but with 1-second cadence. The total power dynamic spectrum is shown in Figure 1. The nominal full-width-half-maximum (FWHM) spatial resolution of this observation is elliptical, with a major axis of $180''/f_{\text{GHz}}$ and a minor axis of $45''/f_{\text{GHz}}$. During the CLEAN imaging process, a circular restoring beam of FWHM $112''.5/f_{\text{GHz}}$ was used. This corresponds to a beam size decreasing from $37''.5$ at 3 GHz to $6''.3$ at 18 GHz.

3. DIAGNOSTICS OF THERMAL PLASMA AND NON-THERMAL ELECTRONS DERIVED FROM HXR OBSERVATIONS

3.1. *Fermi*/GBM data

Solar flare observations with *Fermi*/GBM in the energy range 8 keV–40 MeV provide information on properties of both thermal plasma and nonthermal electrons. For our analysis, we select CSPEC data at 128 energy channels, with 4.096 s nominal time resolution and 1.024 s during the burst, provided by the sunward-facing detector n5. The *Fermi*/GBM X-ray data with background subtracted were fitted with an isothermal (`f_vth`) plus a collisional thick target (`f_thick2`) model, using the OSPEX¹ SSWIDL application.

These fits were applied every 20 s from 18:40:00 UT to 18:41:00 UT, at the rise phase of the flare, every 4 s from 18:41:00 UT to 18:44:00 UT, every 20 s from 18:44:00 UT to 18:46:00 UT, and every 60 s from 18:46:00 UT to 18:49:00 UT. The fitted intervals are highlighted by gray graduation areas in Figure 1(a). The two examples of *Fermi*/GBM fits shown in Figure 3 demonstrate a transition from a nonthermal-dominated phase (middle panel) to a thermal-dominated one (right panel), a few seconds after the HXR peak at 18:41:39.9 UT. The time evolution of the fit parameters is shown in Figure 4: the temperature T_{GBM} (a), the emission measure EM_{GBM} (b), the total integrated electron flux F_0 [in units of 10^{35} electrons/s] (c), the low-energy cut-off E_c [keV] (d), and the spectral index δ of the electron distribution function above E_c (e). The figures confirm an existence of a nonthermal component during the HXR peak. The

¹ For OSPEX documentation see <https://hesperia.gsfc.nasa.gov/rhessi3/software/spectroscopy/spectral-analysis-software/index.html>.

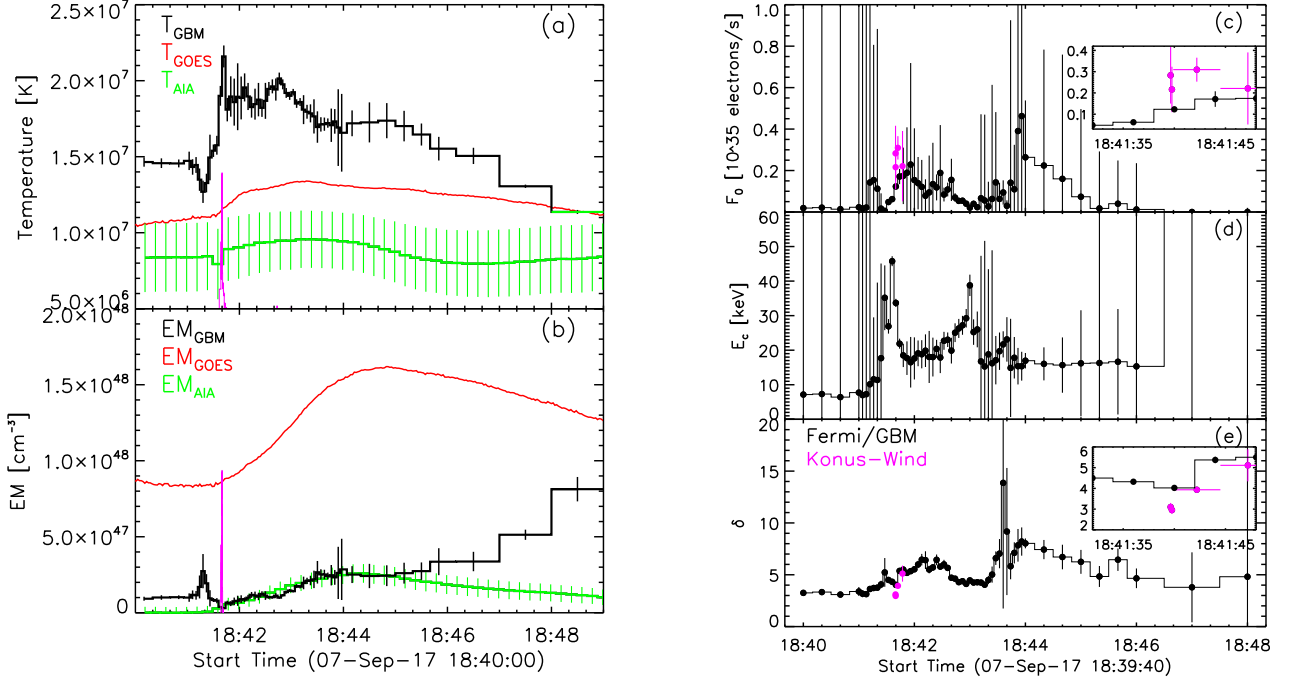


Figure 4. Time evolution of T (a), EM (b), and nonthermal parameters F_0 , E_c , δ (c, d, e) for the 2017-Sep-07 flare. (a) *Fermi*/GBM temperature (black) from the isothermal model for spatially unresolved full solar disk, temperature calculated from *GOES* (red), and AIA temperature (green) from the ROI shown in Fig. 2. (b) *Fermi*/GBM (black), *GOES* (red), and preflare-subtracted AIA (green) emission measure, inferred as described for the upper panel. Magenta histogram indicates the Konus-Wind 18.1–76.5 keV light curve. (c) Total integrated electron flux F_0 , (d) low-energy cut-off E_c , and (e) spectral index δ obtained from the *Fermi* GBM (black histogram) and Konus-Wind (magenta circles) isothermal+thick target fit. Vertical lines indicate the range of 1σ error on the fits.

nonthermal electron flux shows three main peaks corresponding the three peaks of HXR emission. The third electron peak seems the largest, although the uncertainties of the electron flux are rather large, while the spectral slope is softer and E_c is smaller here than in the main peak.

The results of the *Fermi*/GBM spectral model fits are further used to quantify the thermal energy of the hottest component of the flaring plasma, as well as the nonthermal energy of accelerated electrons.

3.2. Konus-Wind data

Konus-Wind provides spectral data for nonthermal hard X-ray and gamma-ray emission in solar flares for energies from ~ 20 keV up to $\gtrsim 10$ MeV (Lysenko et al. 2022). For our analysis, we use the Konus-Wind data in the trigger mode, which provide 64 energy spectra with 64 ms accumulation time for the first four spectra, which then adaptively increases. To cross-check the *Fermi*/GBM fit results we consider the first six time bins after the Konus-Wind trigger, which cover the HXR peak.

The Konus-Wind background-subtracted data were fitted using OSPEX, similarly to Section 3.1: with an isothermal (`f_vth`) plus a collisional thick target

(`f_thick2`) model. Because Konus-Wind is not sensitive to energies less than ~ 20 keV, we use as fixed input parameters: emission measure $EM = 6 \times 10^{46}$ [cm⁻³], temperature $T = 18.96$ [MK], and energy cut-off $E_c = 18.49$ [keV] obtained from the time interval of the *Fermi*/GBM fit at 18:41:48–18:41:52 UT. An example of the Konus-Wind fit at the HXR peak is shown in Figure 3 left panel. The fit results are plotted with magenta circles in Figure 4c,e. The first four 64 ms bins, accumulated from 18:41:39.637 UT to 18:41:39.893 UT, were grouped onto two 128 ms bins to improve the signal-to-noise ratio. The other two bins have a longer accumulation time of 4.6 and 5.38 s, respectively, from 18:41:39.893 UT to 18:41:44.501 UT, and from 18:41:44.501 UT to 18:41:49.877 UT. The fit parameters during the first two short (128 ms) time intervals are different from those obtained from *Fermi* fits obtained for longer (4 s) time intervals, which might indicate sub-second variations of the nonthermal electron population. The fit results reveal soft-hard-soft spectral shape variability during the main impulsive peak, which is typical for impulsive flares with short-scale nonthermal emission (Grigis & Benz 2004).

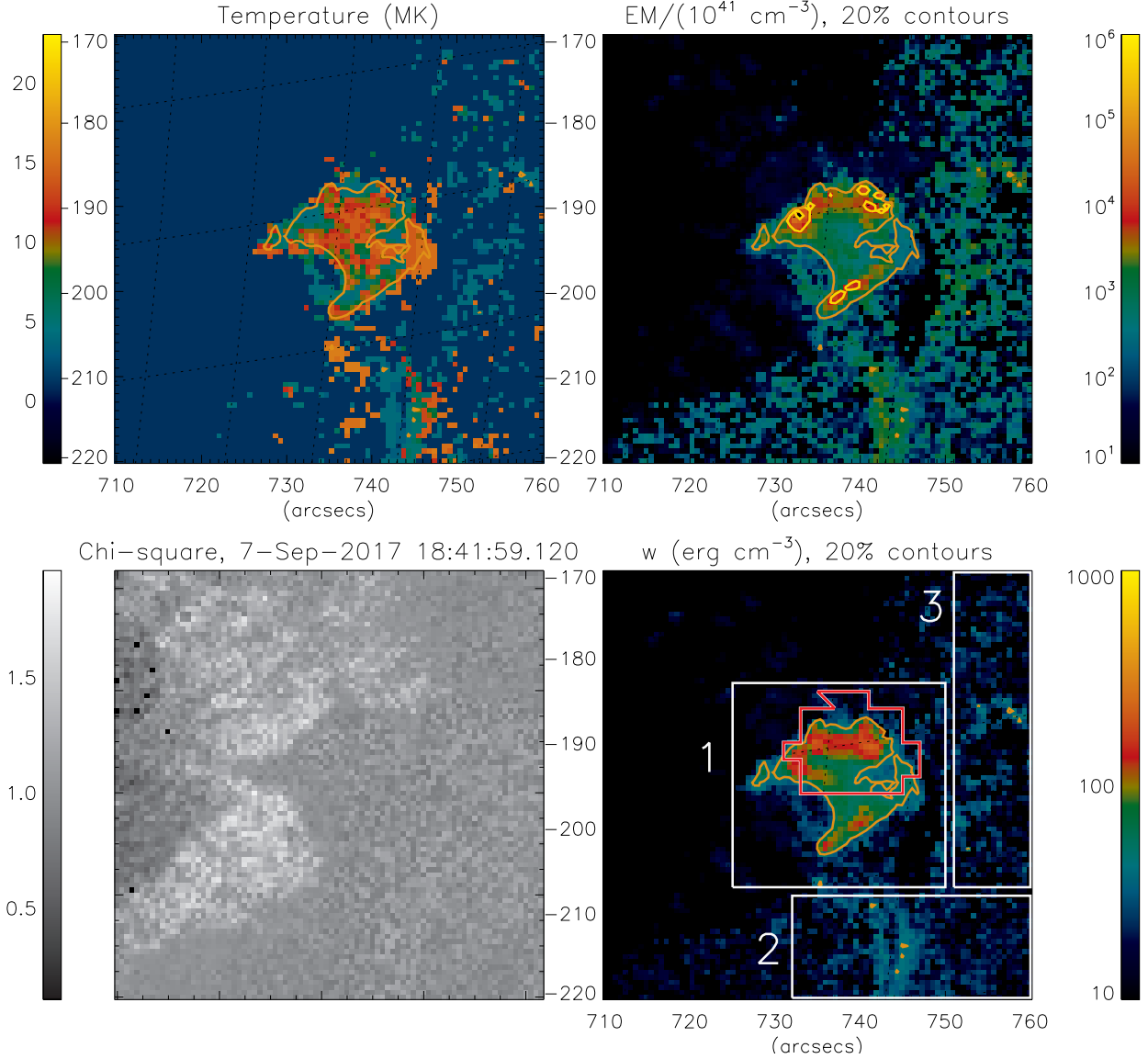


Figure 5. Maps of plasma parameters obtained with the regularized DEM maps based on *SDO*/AIA data: the mean temperature map (top left), the emission measure map (top right), χ^2 map (bottom left), and the thermal energy density map (bottom right) for the 10th time interval (18:41:59–18:42:11 UT). The boxes are labeled with the numbers, their thermal energy evolution is shown in Figure 12. The orange contour shows 20% of the thermal energy density maximum, while yellow contour – 20% of the emission measure peak. The mean temperature map (top left) is plotted only for those pixels where the thermal energy density exceeds 10% of the maximum value for each time interval. Red contour indicates the ROI shown in Figure 7. On-line animation, 22 s, showing evolution of these four panels, is available.

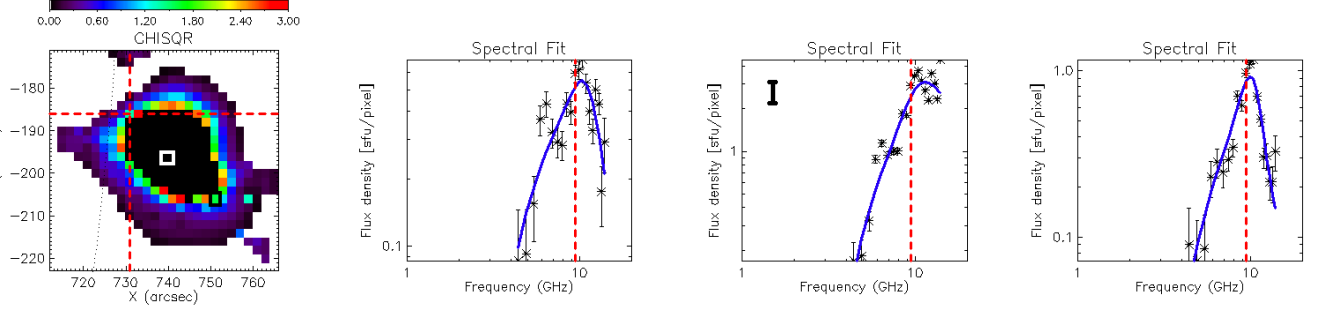


Figure 6. Quality of the spectral fit. Left: χ^2 map for the time frame of 18:41:39.500 UT capped at $\chi^2 = 3$. Other panels: examples of the spatially resolved spectra and their corresponding fits from the locations indicated by the red cursor and white and black squares, respectively. Note a relatively large scatter of the data points in the spectrum taken in the center of the image (white square; third panel), where systematic uncertainties (black vertical bar in the third panel) due to errors in the absolute flux calibration at individual frequencies are larger than the statistical error resulting in a larger χ^2 in that area.

4. THERMAL PLASMA DIAGNOSTICS WITH *SDO*/AIA

To account the thermal plasma of the flare, we use a combination of the six coronal *SDO*/AIA wavebands (see Section 2.3). However, it should be noted that *SDO*/AIA is only faintly sensitive to plasma much hotter than ~ 10 MK and additional constraints are necessary, such as supplementing with X-ray data (e.g., [Motorina & Kontar 2015](#); [Battaglia et al. 2019](#)). Thus, AIA data can only be used to quantify the relatively cool component of the flare plasma.

To infer the emission measure (EM) [cm^{-3}] and temperature [K] from the ROI, we first calculate the DEM [$\text{cm}^{-5} \text{K}^{-1}$] based on a regularization technique ([Tikhonov 1963](#); [Hannah & Kontar 2012](#)). The errors on the AIA data (DN) including the systematic error have been calculated by the formula $DN_{\text{err}} = (DN + (0.2 \times DN)^2)^{0.5}$ (e.g., [Battaglia & Kontar 2013](#)). The evolution of the integral plasma parameters with the minimum preflare emission measure subtracted is given in Figure 4(a, b): the emission measure EM_{AIA} and the mean temperature $\langle T_{\text{AIA}} \rangle$ obtained with DEM from the ROI (see Equations (1-2), [Motorina et al. 2020](#)). After the HXR impulsive peak, both the emission measure and temperature rise. The values of the EM obtained from *Fermi*/GBM and *SDO*/AIA match each other over most of the flare evolution, while they diverge after roughly 18:45 UT. Given that we do not have HXR imaging data, this may be due to X-ray emission outside our area of interest because there maybe more plasma with a modest temperature, which *Fermi* starts seeing once the hot source has cooled down. The temperatures inferred from these two instruments are noticeably different. This difference could be due to the fact that the two instruments are sensitive to different temperatures and, thus, the estimates of the temper-

ature can be biased, or the two instruments may see different sources with similar EM .

The spatially resolved *SDO*/AIA data can provide a detailed diagnostics of the thermal plasma. To infer the DEM maps, the regularized inversion code ([Hannah & Kontar 2013](#)) has been applied to the same *SDO*/AIA dataset. Here we use the methodology described in Section 2.3.2 of [Motorina et al. \(2020\)](#). The obtained DEM maps with the background DEM subtracted are then used to calculate the emission measure maps EM_{ij}^{AIA} [cm^{-3}], the mean temperature maps $\langle T_{ij}^{\text{AIA}} \rangle$ [K], and the thermal energy density w_{ij}^{AIA} [erg cm^{-3}] for all (i, j) pixels (see Eq.(3-5), [Motorina et al. 2020](#)). To estimate w_{ij}^{AIA} , the adopted length along the line of sight (LOS) $l_{\text{depth}} = d_{\text{depth}} \times 0.6 \times 7.25 \times 10^7$ [cm], where $0.6''$ is the AIA pixel size, 7.25×10^7 is the length of $1''$ in cm, while $d_{\text{depth}} = d_{\text{width}} = 5$ [px] has been taken as the mean loop width seen in the EM map for the time interval 18:42:11–18:42:23 UT. Figure 5 shows the 9th time interval (18:41:59–18:42:11 UT) of the animated version of EM^{AIA} , $\langle T^{\text{AIA}} \rangle$, and w^{AIA} maps, along with the chi-squared map (bottom left), which was less than 2 for all considered times indicative of an overall acceptable fitting. The mean temperature derived from the DEM maps, see animated Figure 5, is around 4 MK during the HXR peak time, increases to ~ 15 MK after it, and then slowly decreases. The EM and the thermal energy density sharply increase just after the nonthermal HXR peak time and then slowly decrease. The maximum value of the emission measure was $6 \times 10^{46} [\text{cm}^{-3}]$.

5. FLARE DIAGNOSTICS FROM MICROWAVE OBSERVATIONS

5.1. Overview

We performed the model spectral fitting of the EOVS data with $2'' \times 2''$ pixel size and 1 s time step (best time resolution available with EOVS). We at-

tempted several runs of the spectral fit using GSFIT widget (Fleishman et al. 2020). We performed an initial fitting trial over the frequency range < 15 GHz with six free parameters: magnetic field strength B , its angle to the line of sight θ , thermal number density n_{th} , nonthermal number density n_{nth} , spectral index δ , and high-energy cut-off in the electron energy distribution E_{max} ; see supplemental video in Fleishman et al. (2022) for the dependence of the gyrosynchrotron spectrum on these parameters. When E_{max} was well constrained, it clustered around $E_{max} \sim 2$ MeV. We then fixed E_{max} at 2 MeV and performed several fits with five free parameters within the same (< 15 GHz) and restricted (< 13.5 GHz) spectral ranges. The overall results of the spectral fitting are not sensitive to these choices. Here, we employ the spectral fit run with five free parameters and $f_{max} = 13.41$ GHz. Figure 6 gives an example of the χ^2 map and three individual spectra with their fits. Note that systematic uncertainties (mismatches between neighboring spectra data points) exceed the statistical ones (shown as error bars) in the central area of the image.

5.2. Evolving parameter maps

Figure 7 shows examples of the parameter maps and the parameter evolution obtained from the spectral model fitting. All maps contain edge artifacts mostly located outside the selected EOVS reference contour shown in black. These artifacts are known to originate from the frequency-dependent spatial resolution of the array. The fitting reveals two distinct areas (upper left and bottom right), where some of the fit parameters are different, which we interpret as a signature of two distinct flaring loops. In some of the maps, these areas are separated by a sharp line containing artifacts; likely, due to sharp changes of some physical parameters between these two areas.

The magnetic field is remarkably similar in these two sources being within 500–600 G. The magnetic field does not show any prominent evolution during the burst. The thermal number density is also not much different between those two areas, $n_{th} \sim 10^{11} \text{ cm}^{-3}$. Non-thermal electron number densities above the adopted low-energy cutoff $E_{min} = 15$ keV are different between the two sources: it is about 10^8 cm^{-3} in the upper-left source, while 10^{10} cm^{-3} in the bottom-right source. The spectral indices are also different such as the upper-left spectra are harder than the bottom-right ones.

These fit results show a remarkable soft-hard-soft spectral evolution during the main radio burst at both sources with the range of δ variation from 15 down to 3 and then back to 15. Interestingly, this δ variation is

accompanied by apparently unexpected anti-correlation between the total number of nonthermal electrons and the radio flux, such as this number density reaches a minimum at the flare peak time. This is, likely, an artifact of the arbitrary choice of $E_{min} = 15$ keV or of a deviation of the actual electron spectrum from the adopted here single power-law. Indeed, the microwave spectrum is mostly sensitive to nonthermal electrons with energies much larger than $E_{min} = 15$ keV. Given the prominent hardening of our model spectrum at the flare rise phase, the number density of electrons above 100 keV correlates with the microwave flux in agreement with the common sense, as illustrated in Figure 8.

6. MODELING OF THE FLARING LOOPS WITH GX SIMULATOR

We employed the automated model production pipeline (AMPP, Nita et al. 2023) to create a 3D magnetic data cube based on nonlinear force-free-field (NLFFF) extrapolation constrained by an *SDO*/HMI vector magnetogram taken on 18:34:41 UT (target time was 18:40 UT) prior the flare. This data cube was then used to create a flare model by selecting the designated flare flux tubes to be populated with nonthermal electron components and thermal plasma. An apparent complication in creation this model is that the magnetic field is very complex spatially at the flare site; see Figure 9. There are many field lines that intersect in the projection to the flare sources; thus, creating an ambiguity in the selection of the flaring flux tubes for modeling. To double check the validity of our modeling approach, we also created a NLFFF data cube after the flare that was found to display essentially the same connectivity, which demonstrates that the magnetic field morphology did not change significantly during this flaring episode.

Following the microwave diagnostics, Section 5.2, the model we created contains two adjacent flux tubes, which originate from two northern footpoints located very close to each other. However, their connectivities are very different from each other: their southern footpoints are located far away from each other such as their loop tops project onto two distinct microwave sources. In addition, we added a third flux tube that has a magnetic field about 20 G at the loop top and produces a gyrosynchrotron component with the spectral peak around 2.5 GHz, which is used to account for the spectral flattening at low frequencies. These flux tubes are then populated with thermal and nonthermal electrons as guided by the GSFIT results and the AIA and Fermi data and then fine-tuned, by trials and errors, to match the microwave spectral and imaging data and X-ray spectral data; an overview of the final model,

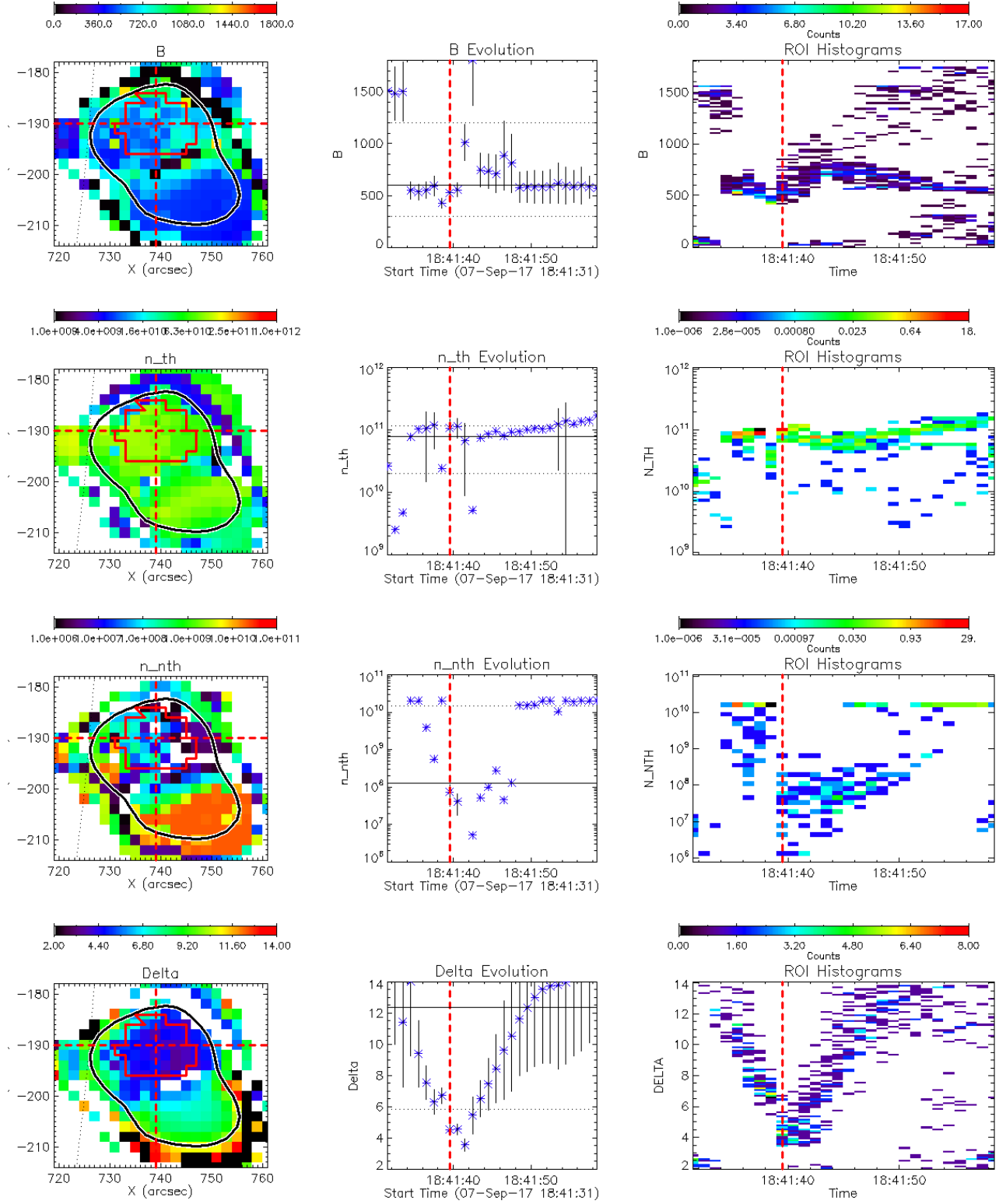


Figure 7. Inferred Parameters and Their Evolution. Top Row: Magnetic field strength. Second Row: Thermal electron number density. Third Row: Non-thermal electron number density. Bottom Row: Non-thermal electron power-law index. Left Column: Parameter maps corresponding to a specific time frame (18:41:39.500 UT). Each map includes the 15% contour (in black) of the EOVS 10.41 GHz microwave map, the boundary defining the selected region of interest (ROI) in red, and the position of a chosen pixel within this ROI (indicated by red-dotted lines). Middle Column: Evolution of the fit parameters for the selected ROI pixel (blue symbols) along with their corresponding median values (horizontal black line). Right Column: Evolution of parameter distributions for all pixels of the selected ROI, corresponding to the same time frames as shown in the middle column plots. In both the middle and right columns, vertical dotted red lines highlight the selected time frame of the maps displayed in the left column. The animated version, 15 s, of this figure is available, which shows evolution of the parameter maps, such as displayed in the left column of this figure, over the entire flare duration.

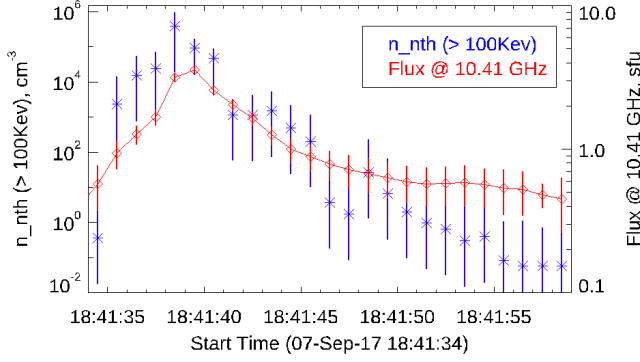


Figure 8. Evolution of the nonthermal number density above 100 keV and fit uncertainties (blue lines and symbols) in the pixel marked by the cursor in Fig. 7 computed from the spectral fit results shown in that figure. The EOVS flux at 10.41 GHz measured in the same pixel is overlaid for comparison (red lines and symbols).

Figure 10, is given in Table 1. Figure 10 displays a visualization of the 3D model by showing three involved flux tubes and spatial distributions of the nonthermal electrons inside them. It also shows synthetic-to-observed microwave image comparison at three different frequencies as well as observed and model microwave spectra at the flare peak time. The microwave emission from shorter loops 1 & 2 and longer loop 3 are shown separately to demonstrate that loop 3 contribution is only significant at the lowest frequencies. Table 1 shows some global parameters of the 3D model obtained either by direct inspection of the model geometry and numeric input or by integration over the flaring loops involved.

7. COMPARISON BETWEEN THE MAGNETIC FIELD MODEL AND SPECTRAL FITTING

To make a comparison between the magnetic field derived from the microwave model spectral fitting with that in the 3D model, we compute the maps of the magnetic field $B_{weighted}(x, y)$ in the model weighted with the 3D spatial distribution of nonthermal electrons $n_{nth}(x, y, z)$ by sampling the model volume over all lines of sights

$$B_{weighted}(x, y) = \frac{\int_0^{h_{max}} B(x, y, z) n_{nth}(x, y, z) dz}{\int_0^{h_{max}} n_{nth}(x, y, z) dz}, \quad (1)$$

and then compare these maps with those obtained from the model spectral fitting; see Figure 7. This weighting is relevant for the comparison because the magnetic field inferred from the microwave spectral fitting is an aver-

aged field over the line of sight segment occupied by the emitting nonthermal electrons.

Figure 11 shows the magnetic field and, for completeness, also the nonthermal and thermal densities, in the model volume sampled with the spatial distribution of the nonthermal electrons, where the flux tube 3 was excluded. The reason for the exclusion is that this flux tube contributes only at low frequencies, while the spectral fitting is dominated by a higher frequency portion of the spectrum; thus, the outcome of the spectral fitting is mainly relevant for comparison with flux tubes 1 and 2. This figure shows that the magnetic fields in the adjacent portions of these flux tubes are comparable to each other, ~ 500 G and also to the range of magnetic field values obtained from the model spectral fitting in Figure 7. Two other maps show similar ranges of parameter variation as shown in Figure 7. In a general case, having gyrosynchrotron emission from two different, closely located flux tube would result, due to smearing of these contributions by the finite instrumental PSF, in broadened spatially resolved spectra indicative of an inhomogeneous source, whose fitting with the uniform source cost function could be problematic. In our case, however, the ranges of the magnetic field in these two flux tubes are similar. Likely, this is why the fits are generally successful and the derived magnetic field values show rather smooth spatial behavior.

8. ENERGY PARTITIONS AND EVOLUTION

8.1. Quantification of the thermal energy with EUV data

The total AIA-derived thermal energy of the flare from the ROI is obtained from the thermal energy density maps w_{ij}^{AIA} described in Section 4:

$$W_{th}^{AIA}(t) = S_{px} l_{depth} \sum_{i=1}^{N_{px}} \sum_{j=1}^{N_{px}} w_{ij}^{AIA}(t) [\text{erg}]. \quad (2)$$

The evolution of the thermal energy W_{th}^{AIA} with subtracted minimum preflare value of $W_{th, min}^{AIA} = 1.78 \times 10^{28}$ [erg] from the non-flaring pixels in the ROI is shown in Figures 12 and 13.

The animated Figure 5 demonstrates that, beside the evolution of the main flaring source (in box #1), there is some dynamics in the bottom (#2) and right (#3) boxes (outlined and numbered in the Figure). It is unclear whether this dynamics is related to the flare, or independent. To estimate the contribution of all boxes to the thermal energy, we show them together with the contribution W_{th}^{AIA} from the ROI in Figure 12. In all cases, the minimum preflare energy from the corresponding box or

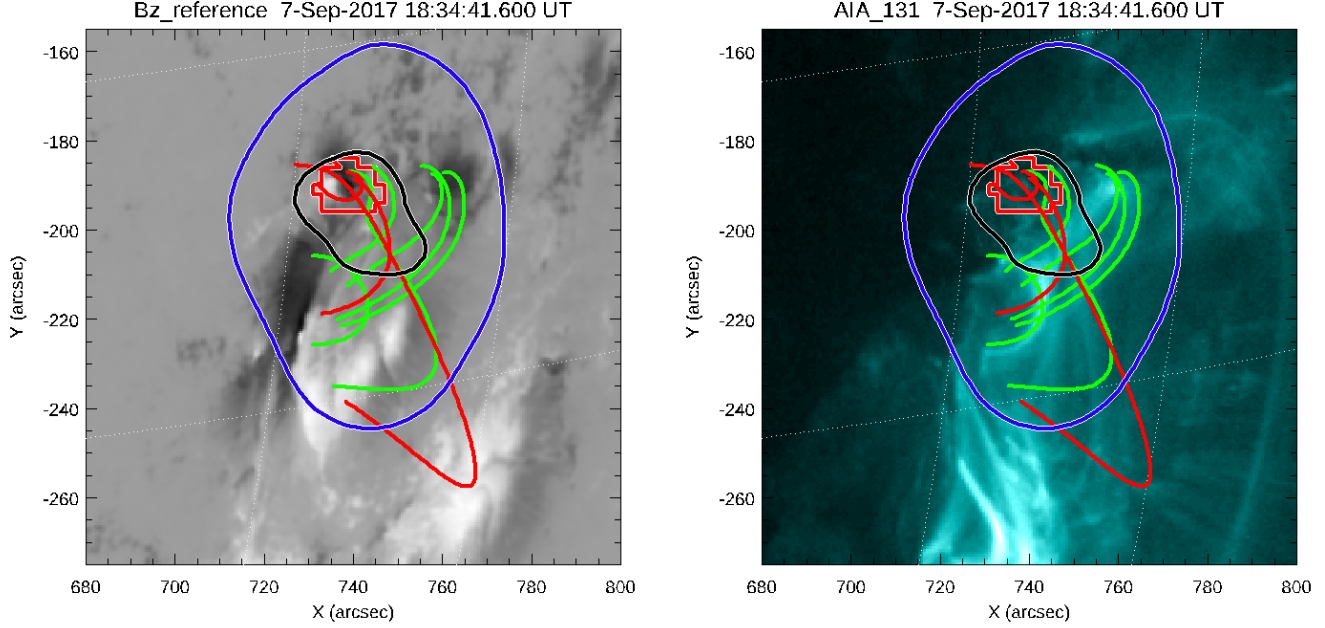


Figure 9. Visualization of 3D model connectivity. Left: three red lines show the axes of three flux tubes used for emission simulation shown in Fig. 10 and several additional closed field lines (green) to emphasize the complexity of the connectivity on top line-of-sight photospheric magnetic field. We also show the ROI (red) and EOVS 10.41 GHz contour (black) same as in Fig. 7 as well as an additional EOVS 3.41 GHz contour (blue). Right: same lines and contours are shown on top of 131 Å image. These lines show consistency of the magnetic model with the bright EUV structures.

ROI was subtracted. Figure 12 shows that the contribution of the boxes #2 and #3 is small compared to the flaring box #1; however, they show a slight increase with time that correlates with the behavior of box #1. This may indicate that, although the main energy release occurs in box #1, the flaring process expands to a larger area. Thus, to take these processes into account, further we use the value of the thermal energy $W_{\text{th}}^{\text{AIA}}$ from the ROI (see Figure 13) which reaches a peak value of about 5.3×10^{28} [erg] during the 18:43:47-18:43:59 UT interval.

8.2. Quantification of the thermal energy with X-ray data

The *Fermi*/GBM spectral model fits can be used to quantify the thermal energy of the hot component ($\gtrsim 20$ MK) of the flaring plasma in a similar way to the estimate reported by Motorina et al. (2020). To account for the thermal energy detected by *Fermi*/GBM, we employ the emission measure and temperature obtained from the *Fermi*/GBM fits (see Section 3.1 and Figure 4):

$$W_{\text{th}}^{\text{GBM}} = 3k_B T_{\text{GBM}} \sqrt{EM_{\text{GBM}} \times V} \text{ [erg]}, \quad (3)$$

where V is the volume of the corresponding thermal source. Here we cannot estimate the hot loop volume from the data directly, due to the lack of X-ray imaging

data. Instead, we rely on the volume of the hottest loop, $V = 1.49 \times 10^{26}$ [cm³] (Loop 2; see Table 1), determined from the 3D model devised in Section 6. The evolution of the *Fermi*/GBM-derived thermal energy $W_{\text{th}}^{\text{GBM}}$ is shown in black in Figure 13. The time history of the estimated thermal energy has a similar shape to the nonthermal energy deposition, which turns sufficient to account the observed plasma heating. We note, however, that this conclusion is based on our estimate of the X-ray source volume from the 3D model rather than from imaging. Indeed, given the lack of X-ray imaging data, we might have incorrectly ascribed the hottest plasma to loop 2; it is possible that another, smaller or bigger loop with proportionally smaller/larger volume, is in fact the main contributor to the thermal X-ray emission. In this case, the estimate of the thermal energy would be proportionally smaller/larger than that shown in the Figure.

8.3. Quantification of the nonthermal energy with X-ray and microwave data and 3D modeling

The nonthermal energy W_{nth} deposited in the flaring volume during 18:40:00-18:49:00 UT versus time was computed as a cumulative sum using the parameters from the *Fermi*/GBM fits:

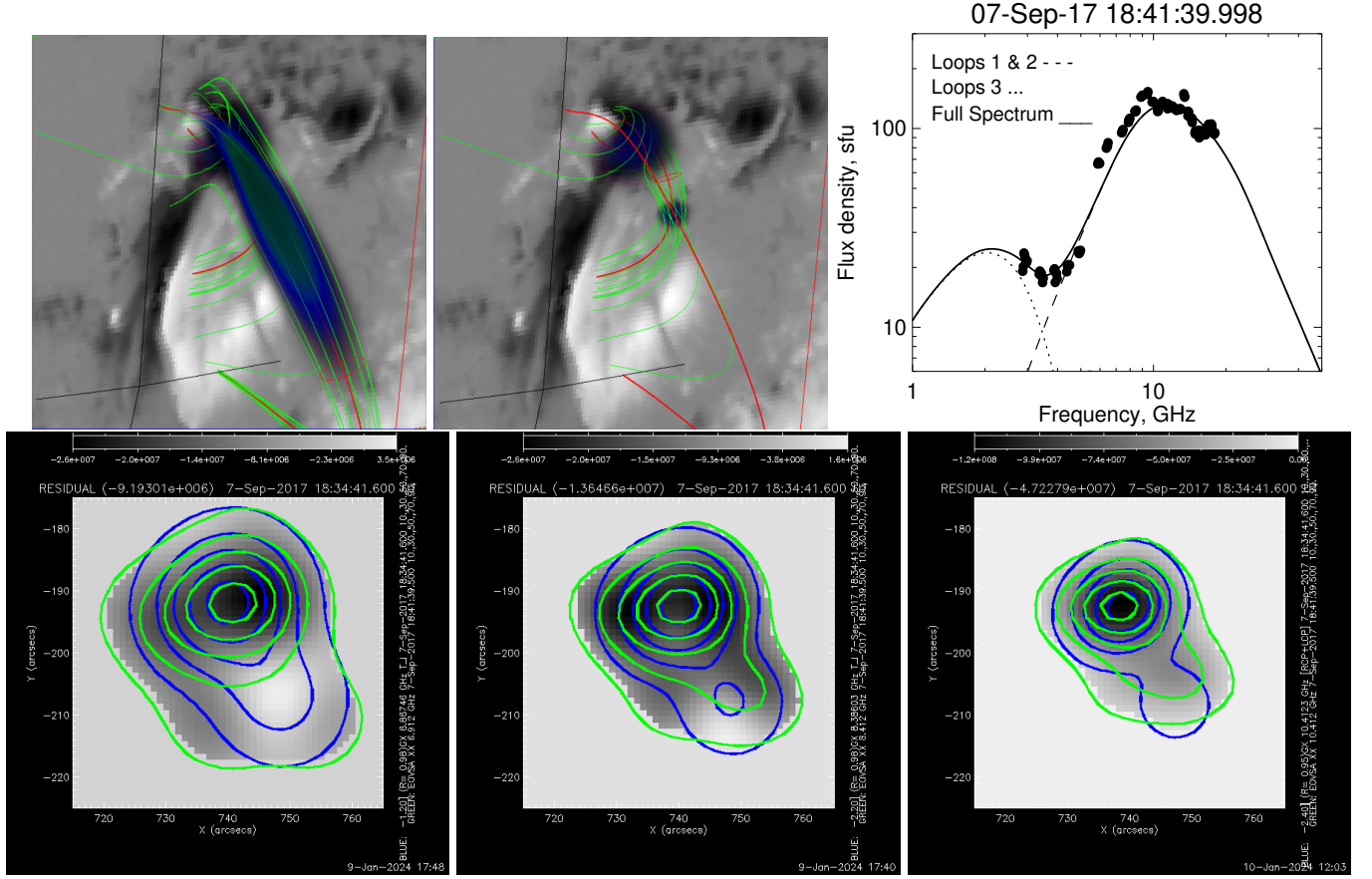


Figure 10. Visualization of the 3D model. Three flux tubes are shown on top of B_z magnetogram with sets of green lines, while their axes are shown with red lines. The bluish volume shows spatial distribution of the nonthermal electrons in these flux tubes. The nonthermal electron distribution in flux tube 2 is hidden under that in flux tube 3, which is excluded in the second panel (the axis of the excluded flux tube is shown as a long red line) to illustrate that. Top right panel shows model-to-data spectral comparison: EOVSA total power data are shown with circles and the solid line shows the model spectrum integrated over the field of view shown in the previous panels; the two other lines show the contributions from flux tubes 1 & 2 (dashed line) and 3 (dotted line). Bottom row shows comparison between synthetic (blue) and observed (green) microwave images at three different frequencies on top of their corresponding residuals within a $50'' \times 50''$ FOV.

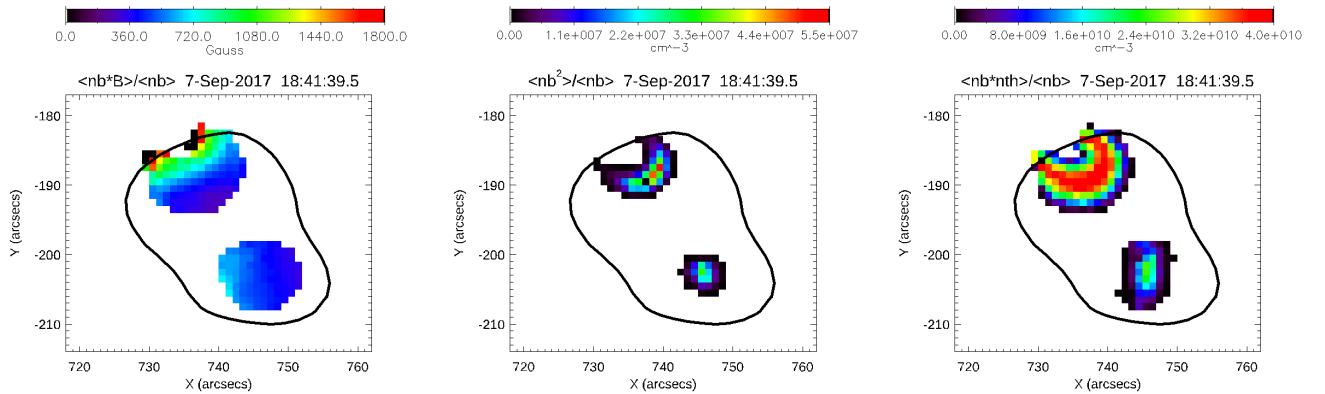


Figure 11. Maps of the weighted magnetic field $B_{weighted}(x, y)$, and nonthermal and thermal number densities for the model introduced in Figure 10 with flux tube 3 excluded shown in the same FOV as the parameter maps in Fig. 7. The black contour shows 15% level of EOVSA emission at 10.41 GHz 18:41:39.5 UT same as in Fig. 7.

Table 1. Summary of the 3D model

Parameter	Symbol, units	Loop 1	Loop 2	Loop 3
<i>Geometry:</i>				
Length of the Central Field Line	l , Mm	15	32	126
Looptop magnetic field	B , G	458	386	23
Footpoint 1 magnetic field	B , G	2422	2033	353
Footpoint 2 magnetic field	B , G	2248	1940	1907
Model Volume; $[\int n_0 dV]^2 / \int n_0^2 dV$	V , cm^3	1.80×10^{26}	1.49×10^{26}	3.67×10^{27}
<i>Thermal Plasma:</i>				
Total Electron Number, $\int n_0 dV$	N_0	5.01×10^{36}	2.13×10^{36}	1.27×10^{36}
Emission Measure, $\int n_0^2 dV$	EM , cm^{-3}	1.39×10^{47}	3.05×10^{46}	4.37×10^{44}
Mean Number Density, EM/N_0	n_{th} , cm^{-3}	2.78×10^{10}	1.43×10^{10}	3.45×10^8
Temperature	T , MK	7	24	22
Thermal Energy	W_{th} , erg	1.45×10^{28}	2.12×10^{28}	1.15×10^{28}
<i>Nonthermal Electrons:</i>				
Total Electron Number, $\int n_b dV$	N_b	8.58×10^{32}	2.96×10^{32}	4.73×10^{34}
Mean Number Density, $\int n_b^2 dV / N_b$	n_{nth} , cm^{-3}	3.73×10^7	2.55×10^7	2.44×10^8
PWL Energy Range	E , MeV	0.015 – 1.0	0.015 – 10.	0.020 – 0.50
PWL Spectral Index	δ	3.20	3.50	3.55
Nonthermal Energy	W_{nth} , erg	3.78×10^{25}	1.18×10^{25}	2.49×10^{27}

^aThis model roughly matches the X-ray spectrum at 18:41:38 — 18:41:42 UT and perfectly at 18:41:46 UT and also complies with the AIA-derived EM constraints.

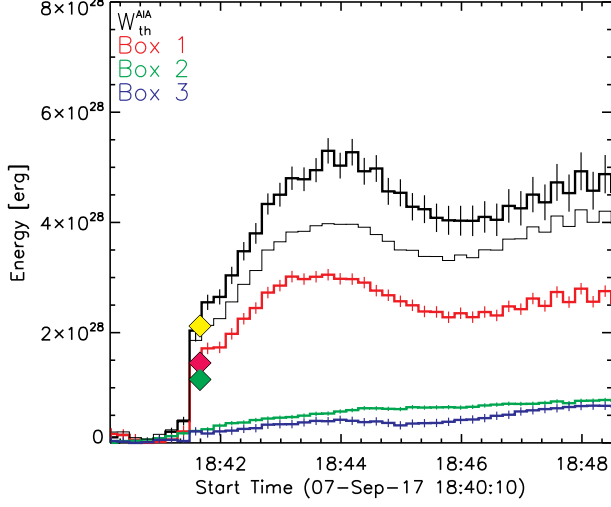


Figure 12. Evolution of the thermal energy $W_{\text{th}}^{\text{AIA}}$ computed from the DEM maps inside the ROI shown in Figure 2 (black line) and three boxes (red, green, and blue lines) outlined by numbers in Figure 5. The sum of three boxes is shown in thin black line. The scarlet, yellow, and green diamonds indicate the model values of thermal energies in Loops 1, 2, and 3, respectively; see Table 1.

$$W_{\text{nth}}^{\text{GBM}} = \int_{-\infty}^t F_0 E_c \frac{\delta - 1}{\delta - 2} dt \text{ [erg]}, \quad (4)$$

where F_0 , E_c , and δ are the thick target parameters shown in Figure 4c-e (see Section 3.1). $W_{\text{nth}}^{\text{GBM}}$ is shown in dark yellow in Figure 13.

We compare this energy deposition with the one estimated using the data-validated 3D model following the approach outlined by (Fleishman et al. 2021). Specifically, using the nonthermal energy estimated at a selected time frame, see Table 1, we can estimate the total nonthermal energy deposition during the main flare peak duration $\tau \approx 8$ s if we know the escape time τ_{esc} of the nonthermal electrons from the source. Fleishman et al. (2021) estimated the escape time as the time delay between the HXR and microwave light curves. In our case, there is no measurable time delay within the available EOVSa time resolution of 1 s. Therefore, we can only estimate an upper bound of the escape time to be $\tau_{\text{esc}} < 1$ s and, thus, the lower bound of the nonthermal energy deposition $W_{\text{nth}} > 2.4 \times 10^{28}$ erg, which is consistent with the $W_{\text{nth}}^{\text{GBM}}$ estimated above, see Figure 13.

9. DISCUSSION

9.1. Summary of main findings

Here we performed a multi-instrument and multi-wavelength study of a 2017-Sep-07 “cold” solar flare. The

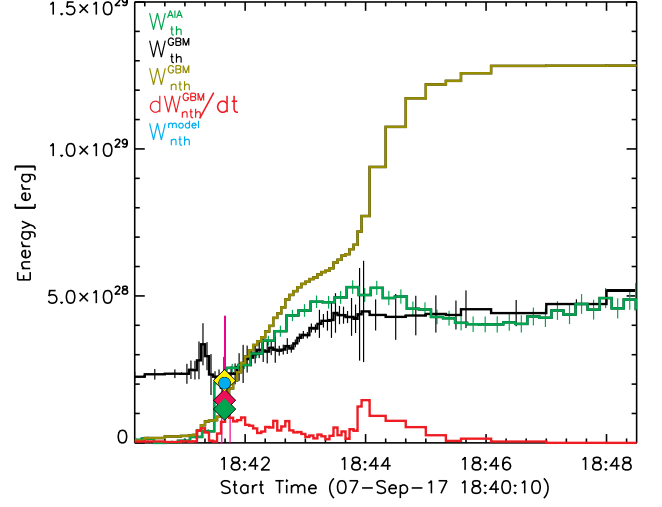


Figure 13. Evolution of energy components in the 2017-Sep-07 flare. The thermal energy $W_{\text{th}}^{\text{AIA}}$ computed from the ROI of the AIA DEM maps is shown in green. The thermal energy $W_{\text{th}}^{\text{GBM}}$ deduced from the thermal part of the *Fermi*/GBM fits assuming flux tube 2 volume in the 3D model is shown in black. The cumulative nonthermal energy deposition $W_{\text{nth}}^{\text{GBM}}$ obtained from the nonthermal part of the *Fermi*/GBM fits is shown with the dark yellow histogram, while the red histogram shows the rate of *Fermi*/GBM nonthermal energy deposition $dW_{\text{nth}}^{\text{GBM}}/dt$ (arb. units). The total nonthermal energy input inferred from the three loops of the 3D model is shown by a light-blue circle. Magenta curve shows the *Konus-Wind* 18.1-76.5 keV light curve. The scarlet, yellow, and green diamonds indicate the model values of thermal energies in Loops 1, 2, and 3, respectively; see Table 1.

uniqueness of this flare compared with other cold solar flares reported so far is the microwave imaging spectroscopy available from EOVSa. This new data set permitted us to obtain evolving parameter maps of physical parameters, including the magnetic field in the coronal portion of the solar flare, and, thus, much better constrain its magnetic structure and plasma environment.

We found that neither the magnetic field nor the plasma density show prominent evolution during the course of the flare, unlike the powerful 2017-Sep-10 eruptive flare produced in the same active region (Fleishman et al. 2020). On the contrary, the nonthermal electron population shows a prominent soft-hard-soft spectral evolution with much stronger variation of the spectral index than typically reported from the X-ray diagnostics.

We estimated the thermal energy evolution constrained by the EUV and X-ray data, as well as nonthermal energy deposition constrained with the X-ray and microwave data and 3D modeling. We found that the

thermal energies are highly correlated with the nonthermal energy deposition. This implies that the observed thermal energy signatures are the response to the deposition of the nonthermal energy. We conclude that there was no direct plasma heating in this flare and that the entire thermal emission was due to the plasma's response to the nonthermal energy deposition.

9.2. Comparison with other cold flares

Let us compare the 2017-Sep-07 cold flare with previously studied cases. A key question is how much and where exactly the free magnetic energy has been released to drive the flare. In some of the previous studies, this was evaluated using 3D magnetic extrapolations before and after the flare; for example, [Fleishman et al. \(2021\)](#) did not find any measurable change in the magnetic energy due to the flare within uncertainties of the models. In our case, we directly measured the coronal magnetic field in the flaring volume. Although some variations are visible in the evolving magnetic field maps, the analysis does not reveal any systematic or statistically significant trends. The uncertainties of the magnetic field in Figure 7 are about 100 G or larger. The ROI shown in that figure inscribes about 50 pixels, which corresponds to the source volume of $V \approx 6 \times 10^{26} \text{ cm}^3$. Therefore the uncertainty in the magnetic energy within the ROI is

$\Delta W_B \sim 2.5 \times 10^{29} \text{ erg}$, which is one order of magnitude larger than the energy needed to drive this flare. This is consistent with the lack of detectable decrease of the magnetic field in this event, in contrast with large flares ([Fleishman et al. 2020](#)).

The morphology of this flare is overall similar to other cold flares, as it includes three distinct, presumably interacting, flaring loops. The energy partitions between these loops in the developed model are summarized in Table 1. Interesting, that most of the energy belongs to flux tube 3, while the dominant contributors to the microwave emission are loops 1 and 2.

The nonthermal energy deposition is sufficient for the thermal energy quantified by the AIA and *Fermi* data; Figure 13. We conclude that the scenario in which the entire thermal response in this flare is driven by non-thermal energy deposition is likely, similar to other cold flares.

This work was partly supported by NSF grants RISE-2324724 and AGS-2425102 and NASA grant 80NSSC23K0090 to New Jersey Institute of Technology, GM (X-ray and EUV analysis) was supported by RSF grant No. 20-72-10158. We are thankful to Alexandra Lysenko for fruitful discussions of the *Konus-Wind* data.

REFERENCES

- Aptekar, R. L., Frederiks, D. D., Golenetskii, S. V., Ilynskii, V. N., Mazets, E. P., Panov, V. N., Sokolova, Z. J., Terekhov, M. M., Sheshin, L. O., Cline, T. L., & Stilwell, D. E. 1995, *SSRv*, 71, 265
- Battaglia, M. & Kontar, E. P. 2013, *ApJ*, 779, 107
- Battaglia, M., Kontar, E. P., & Motorina, G. 2019, *ApJ*, 872, 204
- Benz, A. O. 2008, *Living Reviews in Solar Physics*, 5, 1
- Caspi, A. & Lin, R. P. 2010, *ApJL*, 725, L161
- Fleishman, G. D., Gary, D. E., Chen, B., Kuroda, N., Yu, S., & Nita, G. M. 2020, *Science*, 367, 278
- Fleishman, G. D., Kleint, L., Motorina, G. G., Nita, G. M., & Kontar, E. P. 2021, *ApJ*, 913, 97
- Fleishman, G. D., Nita, G. M., Chen, B., Yu, S., & Gary, D. E. 2022, *Nature*, 606, 674
- Fleishman, G. D., Pal'shin, V. D., Meshalkina, N., Lysenko, A. L., Kashapova, L. K., & Altyntsev, A. T. 2016, *ApJ*, 822, 71
- Gary, D. E., Chen, B., Dennis, B. R., Fleishman, G. D., Hurford, G. J., Krucker, S., McTiernan, J. M., Nita, G. M., Shih, A. Y., White, S. M., & Yu, S. 2018, *The Astrophysical Journal*, 863, 83
- Grigis, P. C. & Benz, A. O. 2004, *A&A*, 426, 1093
- Hannah, I. G. & Kontar, E. P. 2012, *A&A*, 539, A146
- . 2013, *A&A*, 553, A10
- Lemen, J. R., Title, A. M., Akin, D. J., Boerner, P. F., Chou, C., Drake, J. F., Duncan, D. W., Edwards, C. G., Friedlaender, F. M., Heyman, G. F., Hurlburt, N. E., Katz, N. L., Kushner, G. D., Levay, M., Lindgren, R. W., Mathur, D. P., McFeaters, E. L., Mitchell, S., Rehse, R. A., Schrijver, C. J., Springer, L. A., Stern, R. A., Tarbell, T. D., Wuelser, J.-P., Wolfson, C. J., Yanari, C., Bookbinder, J. A., Cheimets, P. N., Caldwell, D., Deluca, E. E., Gates, R., Golub, L., Park, S., Podgorski, W. A., Bush, R. I., Scherrer, P. H., Gumm, M. A., Smith, P., Aufer, G., Jerram, P., Pool, P., Soufli, R., Windt, D. L., Beardsley, S., Clapp, M., Lang, J., & Waltham, N. 2012, *SoPh*, 275, 17
- Lin, R. P., Dennis, B. R., Hurford, G. J., et al. 2002, *SoPh*, 210, 3
- Lysenko, A. L., Altyntsev, A. T., Meshalkina, N. S., Zhdanov, D., & Fleishman, G. D. 2018, *ApJ*, 856, 111

- Lysenko, A. L., Ulanov, M. V., Kuznetsov, A. A.,
Fleishman, G. D., Frederiks, D. D., Kashapova, L. K.,
Sokolova, Z. Y., Svinkin, D. S., & Tsvetkova, A. E. 2022,
ApJS, 262, 32
- Lysenko, A. L., White, S. M., Zhdanov, D. A., Meshalkina,
N. S., Altyntsev, A. T., Motorina, G. G., & Fleishman,
G. D. 2023, ApJ, 954, 122
- Meegan, C., Lichti, G., Bhat, P. N., Bissaldi, E., Briggs,
M. S., Connaughton, V., Diehl, R., Fishman, G., Greiner,
J., Hoover, A. S., van der Horst, A. J., von Kienlin, A.,
Kippen, R. M., Kouveliotou, C., McBreen, S., Paciesas,
W. S., Preece, R., Steinle, H., Wallace, M. S., Wilson,
R. B., & Wilson-Hodge, C. 2009, ApJ, 702, 791
- Motorina, G. G., Fleishman, G. D., & Kontar, E. P. 2020,
ApJ, 890, 75
- Motorina, G. G. & Kontar, E. P. 2015, Geomagnetism and
Aeronomy, 55, 995
- Neupert, W. M. 1968, ApJL, 153, L59
- Nita, G. M., Fleishman, G. D., Kuznetsov, A. A.,
Anfinogentov, S. A., Stupishin, A. G., Kontar, E. P.,
Schonfeld, S. J., Klimchuk, J. A., & Gary, D. E. 2023,
The Astrophysical Journal Supplement Series, 267, 6
- Sui, L., Holman, G. D., & Dennis, B. R. 2006, ApJL, 645,
L157
- Tikhonov, A. N. 1963, Soviet Math. Dokl., 4, 1035
- White, S. M., Thomas, R. J., & Schwartz, R. A. 2005, Sol.
Phys., 227, 231